LASSA: a large area silicon strip array for isotopic identification of charged particles

B. Davin[a], R.T. de Souza[a,b,*], R. Yanez[a,1], Y. Larochelle[a,2], R. Alfaro[a], H.S. Xu[a], A. Alexander[a], K. Bastin[a], L. Beaulieu[a,2], J. Dorsett[a], G. Fleener[a], L. Gelovani[a], T. Lefort[a,3], J. Poehlman[a], R.J. Charity[c], L.G. Sobotka[c], J. Elson[c], A. Wagner[d,4], T.X. Liu[d], X.D. Liu[d], W.G. Lynch[d], L. Morris[d], R. Shomin[d], W.P. Tan[d], M.B. Tsang[d], G. Verde[d], J. Yurkon[d]

[a] Department of Chemistry and Indiana University Cyclotron Facility, Indiana University, Bloomington, IN 47405, USA
[b] Grand Accelerateur d'Ions Lourds DSM-CEA/IN2P3-CNRS, BP 5027, F-14076 Caen, Cedex 5, France
[c] Department of Chemistry, Washington University, St. Louis, MO 63130, USA
[d] NSCL and Department of Physics and Astronomy Michigan State University, East Lansing, MI 48824, USA

Abstract

A new high resolution, charged particle detector array, LASSA, has been developed. LASSA consists of nine individual telescopes that each utilizes a Si–Si–CsI(Tl) stack to provide isotopic identification of fragments ($1 \leqslant Z \leqslant 8$) with good angular resolution over a wide dynamic range in energy. The energy range covered is $E/A = 2.4–140$ MeV for protons and $E/A = 4.8–335$ MeV for ^{16}O ions. The front portion of each telescope is comprised of a 65 μm Si(IP) strip detector backed by a 500 μm Si(IP) strip detector. This second detector provides position information in two dimensions. Behind the second silicon detector is a cluster of four 6 cm thick CsI(Tl) crystals, each read-out by a photodiode. The design, construction, and performance characteristics of this detector telescope are described. © 2001 Elsevier Science B.V. All rights reserved.

---

*Corresponding author. Department of Chemistry, Indiana University, Bloomington, IN 47405, USA. Tel.: +1-812-855-3767; fax: +1-812-855-8300.

E-mail address: desouza@indiana.edu (R.T. de Souza).

[1] Present address: Department of Physics, Faculty of Science, University of Chile, Santiago, Chile.
[2] Present address: Laboratoire de Physique Nucleaire, Departement de Physique, University of Laval, Quebec, Canada G1K-7P4.
[3] Present address: LPC, Universite de Caen, 14000 Caen, France.
[4] Present address: Forschungszentrum Rossendorf e.V., Postfach 510119, 01314 Dresden, Germany.

1. Introduction

It has been recently proposed that the thermodynamic properties of nuclear matter (the nuclear equation-of-state) are sensitive to the N/Z degree of freedom. Theoretical calculations [1] suggest that characterizing the N/Z of fragments formed in a low-density medium, in contrast to the N/Z of fragments emitted from normal density nuclear matter, could provide important information about the nuclear equation-of-state. Dynamical properties (e.g. deflection functions) of the transient systems used to create excited nuclear matter are also influenced by the N/Z of the two colliding nuclei [2]. Initial experimental and theoretical work on N/Z equilibration [3–8] at intermediate energies demonstrates clearly the dynamical and non-equilibrium nature of the short-lived systems formed. More detailed studies, however, require isotopic identification of fragments over a substantially broader range of Z, energy, and angle than is presently possible. In addition, these measurements must be carried out with both good energy and angular resolution in order to investigate multi-particle correlations. The advent of new radioactive beam facilities promises access to beams of extreme N/Z that are presently inaccessible. However, the intensity of the most exotic beams will be always be low, thus necessitating development of high efficiency arrays capable of isotopic identification. In this work, we present initial efforts to develop a modest coverage array capable of isotopic identification of charged particles with $Z \leqslant 8$.

2. Design constraints

An extremely powerful tool in investigating the decay of excited nuclear matter is the fragment–fragment correlation technique [9,10]. This technique has been utilized to investigate the excited state populations of *primary* fragments [11] in order to deduce the temperature of the emitting system, as well as to study the spatial and temporal extent of the emitting source [12,13]. An alternate means of probing the temperature of the excited system is the double-isotope thermometer technique [14,15]. At present, both of these experimental approaches have been limited by the isotopic resolution, angular resolution, and energy resolution, of the experimental data, as well as by kinematic efficiency.

The requirements of good energy resolution ($\leqslant 1\%$), for isotopic identification of intermediate mass fragments (IMF: $3 \leqslant Z \leqslant 20$), and of good angular resolution ($\theta \leqslant 1^{\circ}$), necessary for correlation studies, mandated use of a telescope based upon a semiconductor detector. In addition, if segmented, such devices provide the capability of multiple particle detection at small relative angles within a single telescope.

In order to provide low identification thresholds for low velocity, highly ionizing particles, a 65 µm Si strip detector was selected to be the first element of the telescope, resulting in a threshold of ~ 2.5 MeV/u for ^{4}He and ~ 5 MeV/u for ^{16}O. The strips served both to reduce the detector capacitance and to provide position resolution. Energy measurement of high velocity light charged particles (p, d, t, ^{3}He, ^{4}He, and ^{6}He) necessitated use of a scintillator for which we chose CsI(Tl) crystals, 6 cm thick, read out by photodiodes (PD). This crystal thickness results in a maximum identification energy of $E/A = 140$ MeV for protons and $E/A = 335$ MeV for ^{16}O ions. To measure the scintillation within the CsI(Tl) crystal, we elected to use a photodiode due to its characteristics of excellent linearity over a wide dynamic range, stability over long durations, and compact size. The PD chosen was the Hamamatsu S3204 [16], a 2×2 cm^2 photodiode. The maximum count rate of such a Si–CsI(Tl)/PD telescope is limited, by the long decay constant of the CsI(Tl), to a few kilohertz in order to avoid pile-up in the CsI(Tl) crystal. This rate was sufficient for all the intended experiments. Since energetic light particles deposit very little energy in the 65 µm Si, thus making particle identification by the ΔE–E technique difficult, a second thicker Si strip detector in front of the CsI(Tl) was necessary. The arrangement of the double-stack of Si backed by CsI(Tl)/PD used in LASSA is shown in Fig. 1. This telescope is designed to operate in high vacuum ($P \sim 1 \times 10^{-6}$ Torr) with minimal outgassing.
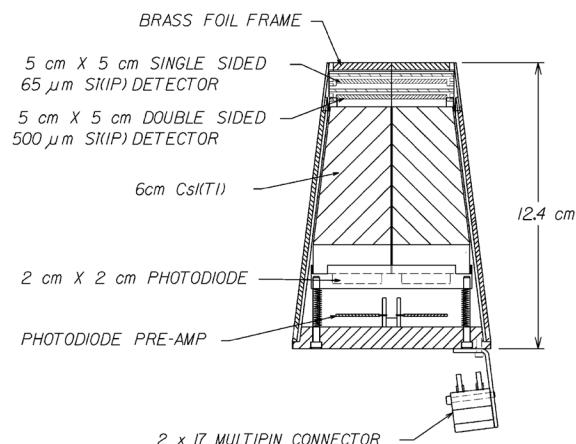
Fig. 1. CAD rendition of a detector telescope (cross-sectional view).

Fig. 2. Photo of a detector with Si–Si section partially removed from the CsI(Tl)/PD section.

The silicon detectors used in LASSA are ion-implanted, passivated devices, Si(IP), (Design W) obtained from Micron Semiconductor [17]. The first detector of the stack is nominally 65 μm thick. The second Si detector is either 500 μm or 1 mm thick depending on the focus of the experiment. The 1 mm Si detector has strips on the front surface (junction side) only while the 500 μm detector has strips on both front (junction) and rear (ohmic) surfaces in orthogonal directions, allowing two-dimensional position information from this detector alone. When the 1 mm detector is used, its strips are oriented orthogonal to the strips in the 65 μm in order to provide two-dimensional position resolution for this configuration. The pitch of the strips (nominally 3 mm with an interstrip SiO_2 isolation of 100 μm) was chosen in order to maintain a modest value of capacitance (~ 250–300 pF/strip) for the thin (65 μm) detector. At the design target-telescope distance of 20 cm, the angular resolution of a strip is $\Delta\theta \sim 0.9°$. The entire detector assembly was housed in two separable aluminum boxes of a trapezoidal geometry. These boxes were designed to provide mechanical support, relative alignment, and electromagnetic shielding of the detectors and photodiode pre-amplifiers, as shown in Fig. 1. The housing was designed and fabricated to contribute as minimally as possible to the dead area of a detector. The total active area of a detector is
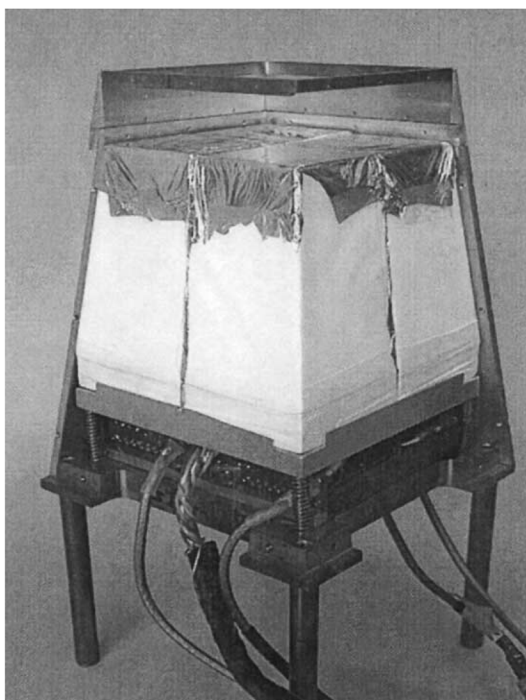
$\sim 75\%$. The inactive area of 25% is divided among the interstrip region (3%), the SiO_2 border on the wafer itself (7.3%), the printed circuit board frame that holds the Si wafer (6.7%), and the aluminum can (8.0%).

The detachable nature of the front Si box and the back CsI(Tl)/PD box allows easy access to either section. In Fig. 2, two sides of both the Si box and the CsI(Tl)/PD box have been removed to show the internal mounting structure. The CsI(Tl)/PD box is mounted on a brass flange from which the relative alignment of all active elements of the telescope is determined.

3. Si detectors

3.1. Mechanical mounting and electrical contacts

Since several of the experiments for which LASSA was designed require close packing of the telescopes in the array, it was necessary to

minimize the dead area surrounding each Si wafer. The commercially available detector frame for a Design-W detector did not allow close packing of the telescope. Therefore, a new frame was designed in which the Si wafer is epoxied into a frame made out of printed circuit board (G-10) with a recessed well. Only 1 mm of this detector frame extends beyond the physical dimension of the Si wafer. This 1 mm border is responsible for the loss of 6.7% of the active area. The challenge of such a minimal detector frame was the extraction of the 16 (or 32 for a double-sided detector) signals. This problem was overcome by the "in-house" development of a flexible cable that is attached permanently to the frame with a low volatility epoxy (Ablestik 84-3) to form an integrated package. The flexible cable provides gold plated pads $(0.062 \times 0.030$ in.^{2}) in the plane of the Si wafer, thus allowing automated wire bonding of the cable to the Si strips.

The flexible cable was fabricated by first printing the desired pad and trace pattern on a sheet of polyimide covered on one side with rolled annealed copper (R/flex 1000) [18] and subsequently etching it, bending it, and epoxying it to the printed circuit board detector frame. The polyimide is 0.002 in. thick with a copper thickness of 0.001 in. (Sheets of electro-deposited copper proved unsatisfactory as they cracked during the bending stage of the fabrication process.) After printing the desired pad and trace pattern, the sheet was then etched using a DirectImaging plotter/etcher [19]. Next, the cable was laminated with a 0.002 in. thick polyimide protective cover (R/flex 1000) on the copper-clad side to prevent accidental shorting of signals. The lamination was achieved by sandwiching the cable and its cover between two 1-in. thick steel plates at a temperature of 175°C for 1.5 h. The resulting cable was then bent with a precision bending fixture and epoxied to the G-10 detector frame. At the other end of the cable, another printed circuit board was attached to allow subsequent mounting of a multipin connector. The entire assembly was cured in an oven for 2 h at a temperature of 125°C. Following a thorough mechanical and electrochemical cleaning, nickel (SIFCO 2080) and then gold (SIFCO 3024) [20] were electroplated onto the
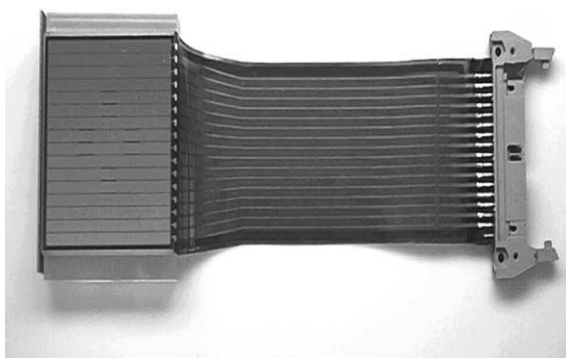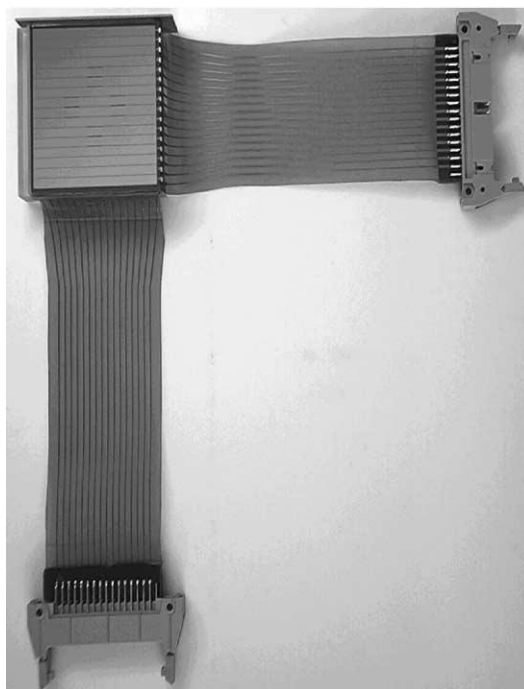

Fig. 3. Photo of a 65 μm single sided detector.

Fig. 4. Photo of a 500 μm double sided detector.

pads using a brush plating technique (e.g. 19 V, 15 mA, 8 min for the gold). Finally, the IDC 34 pin connector (3M 3431-2303) was soldered on. Closeup views of the Si-flexible cable assembly for both the single-sided 65 μm and double-sided 500 μm detectors are provided in Figs. 3 and 4, respectively.

3.2. Measurement of silicon resolution and depletion voltage

Upon delivery of the Si(IP) detectors from Micron Semiconductor, the energy resolution of each strip was measured by scanning the detector with a collimated ^{228}Th α-particle source. A typical spectrum, obtained at $\sim 28°$C, is shown in
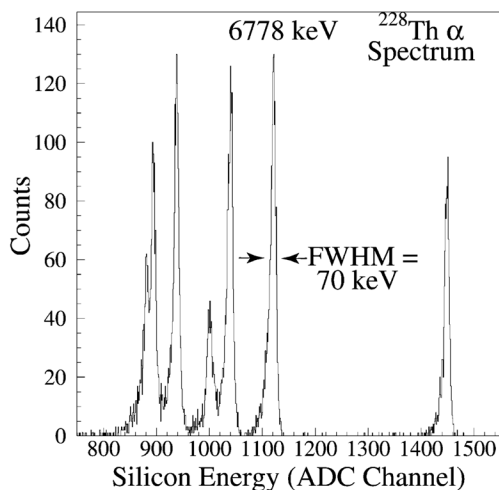

Fig. 5. Alpha spectrum of a collimated ^{228}Th source in one strip of a LASSA detector.

Fig. 5. The strip resolution was recorded based on the FWHM of the 6778 keV peak. (Typical resolution of the two end strips was sometimes worse due to the absence of a guard ring to ensure better voltage isolation for these terminal strips.) Leakage currents upon delivery varied from 0.420 to 9.55 μA for the 500 μm detectors. Large leakage currents, indicative of a low resistance path to ground, generally correlated with poorer resolution. A compilation of the observed FWHM of all the detectors is depicted in Fig. 6. It should be noted that the strip resolution shown in Fig. 6 includes the electronic noise of the test setup. Typically, the electronic noise was 30 keV as measured using a precision pulser. Thus, the most probable resolution of 75 keV measured for a 65 μm detector corresponds to an intrinsic resolution of 69 keV. In Fig. 6, it can also be noticed that the resolution distribution of the back (ohmic side strips) exhibits a tail on the poor resolution side. We hypothesize that this poorer resolution (of some detectors) may be due to lower inter-strip isolation on the ohmic side, inherent to the fabrication process, leading to charge leakage to adjacent strips. Use of implanted p$^+$ isolation strips between adjacent strips on the ohmic side can improve inter-strip isolation.
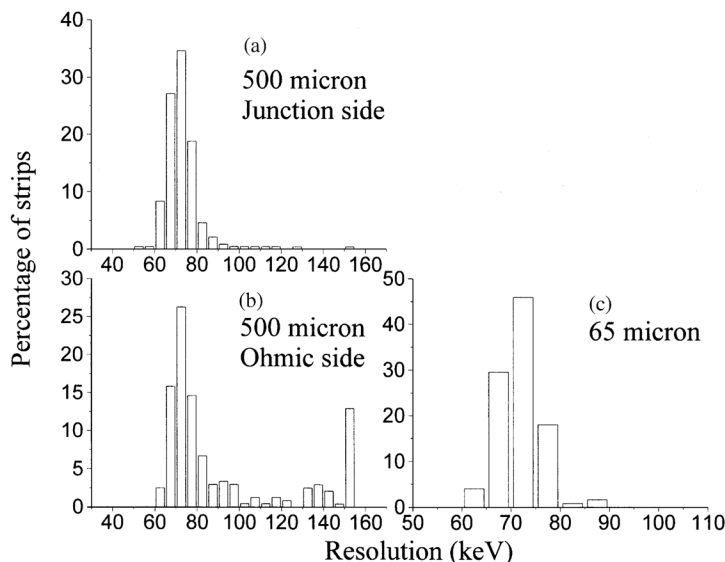

Fig. 6. Statistics of strip resolution.

As it is necessary to fully deplete the detectors in order to achieve complete charge collection, we measured the full depletion voltage for each detector. This voltage was determined by injecting an α particle into the rear surface and maximizing the collected charge as a function of the applied bias. Dead layers on similar detectors have been previously measured [21] to range between 0.5 and 0.75 μm Si equivalent.

4. Electronics

A crucial aspect of this project was the ability to maintain the good energy resolution possible with a Si(IP) detector in any associated electronics. The large number of Si channels in LASSA (432) mandated the development of a low-cost, high-density pre-amplifier. Based upon Monte Carlo energy loss calculations, including straggling, and our design constraint of isotopic resolution up to and including oxygen, we determined the necessary energy resolution to be $\delta E/E = 60\,\text{keV}/6\,\text{MeV}$ for α particles. Maintaining this design constraint for the 432 Si channels of LASSA required that the charge integrating pre-amplifier be capable of operating in vacuum adjacent to the detectors, so as to minimize the influence of cable capacitance.

The large number of channels in LASSA also required development of an integrated shaper/discriminator module that would allow easy control of the LASSA signals (e.g. gain of the slow output and discriminator threshold). It is also vital to measure the long-term stability of these electronics. This requirement necessitated development of a versatile and easily controlled pulsing system. The details of all these electronic elements are described in the following sections.

4.1. Charge integrating pre-amplifier

The quality of the pre-amplifier (PA) used is a critical component in the measured energy resolution of the Si detector. Given the number of channels involved and the space constraints, all pre-amplifiers were constructed using surface mount technology, with the exception of the input field effect transistor (FET) and the load resistor. Discrete components were used for the input FET to allow access to the largest variety of input FETs. To achieve the best possible resolution it is necessary for the input FET to have optimal characteristics (transconductance, slew rate, etc.). Using this approach we were able to limit the size of the pre-amplifier to 0.7×1.0 in.^{2}. A schematic of the pre-amplifier is shown in Fig. 7. The three FETs we tested were the J109 (Siliconix), 2N5434 (InterFET), and the IF9030 (InterFET). The principal characteristics of these FETs are summarized in Table 1. Our tests demonstrated that pre-amplifiers with the IF9030 provided measurably better energy resolution than those with the
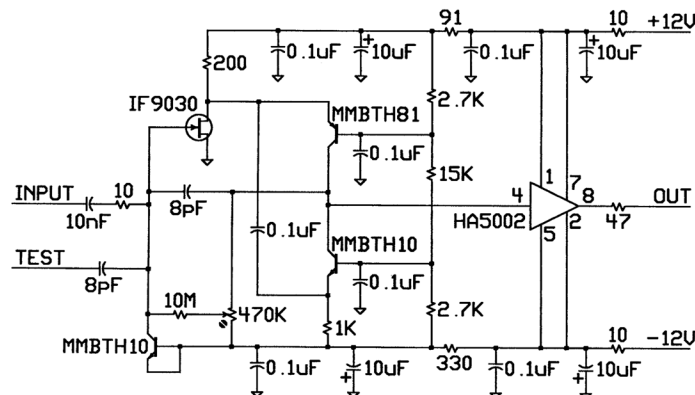
Fig. 7. Electronic circuit diagram of pre-amplifier.

Table 1
Comparison of the characteristics of different FETs tested in the LASSA preamp circuit

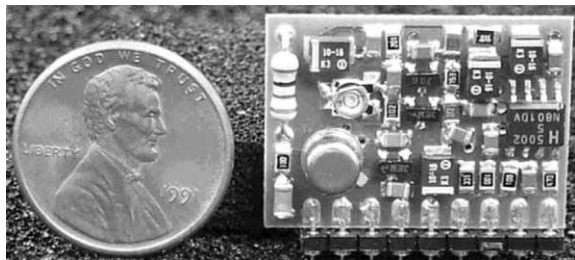| FET	$V_{GS(off)}$ (V)	$r_{DS(on)}$ (Ω)	$I_{D(off)}$ (pA)	t_{on} (ns)
J109	−2 to −6	12	20	4
2N5434	−3 to −9	7	10	2.5
IF9030	−2 to −7	5	10	7

Fig. 8. Photo of a pre-amplifier.

other two FETs. In benchtests, the PA with the IF9030 was able to produce a resolution of 37 keV for a 6 MeV α particle. In measurements with a internal conversion electron from ^{209}Bi we measured an intrinsic resolution of 14 keV. We therefore selected the IF9030 for all strips in which energy resolution was important; i.e. the front strips of the 500 μm detector (EF$_{500}$). For the back strips of the 500 μm detector (EB$_{500}$), which are primarily used for position measurement, we used the 2N5434, which was significantly cheaper than the IF9030. The quality of the output signal was further ensured by use of a high quality isolation buffer amplifier (HA5002). The LASSA charge integrating pre-amplifier is shown on the right-hand side of Fig. 8.

The pre-amplifiers are plugged into a mother-board (16 channels) that provides power, a distributed pulser signal, and the individual detector inputs and outputs. These motherboards, housed in an aluminum box, operate in vacuum with active cooling to dissipate the heat generated. Each pre-amplifier generates ~ 300 mW.

4.2. Silicon processor module

In order to process the Si (and CsI(Tl)/PD) signals efficiently, we developed a double-width CAMAC module consisting of a slow shaper, a timing filter amplifier, a leading edge (LE) discriminator, and a time-to-charge converter all for 16 independent channels [22]. The output of the timing filter amplifier for a Si strip (EF$_{500}$) has a risetime of ~ 25 ns, resulting in a time resolution of 2–3 ns, making fast coincidence timing possible. The timing resolution is limited by the LASSA pre-amplifier. We achieved a risetime of ~ 12–14 ns with a prototype fast pickoff circuit that was not implemented in the final design due to its additional heat dissipation. The CAMAC module also provides an OR output of the discriminators, a linear signal proportional to the number of channels above threshold (MUL), and a pile-up bit. The linear and logic signals are separately multiplexed to an output for inspection purposes. The gain of the slow shaper and the thresholds of the LE discriminators are control-lable via an 8-bit digital-to-analog (D/A) con-verter. Integration and differentiation constants for the slow shaper can be modified by changing plug-in resistors and capacitors in the module. The output polarity of the slow analog signal is selectable by internal jumpers. A functional block diagram of the silicon processor module is shown in Fig. 9.

4.3. Stability measurement

In order to monitor the stability of the electronics over an extended period of weeks, an automated pulsing system was developed at Indiana University [23]. This pulser is stable to within $\sim 0.1\%$ and injects a precise voltage into the test input of each pre-amplifier. A functional block diagram of the IU pulser is shown in Fig. 10. A Master Clock (oscillator of 3.2768 MHz) synchronizes all analog pulses. Two different capacitors are charged to provide pulses for the Si (ΔE_{65}, EF$_{500}$, EB$_{500}$) and CsI(Tl) pre-ampli-fiers separately. The charging rate is controlled by a 12-bit D/A converter that allows remote manipulation of the pulse amplitude. An attenua-tor on each class of signals (ΔE_{65}, EF$_{500}$, EB$_{500}$, and E_{CsI}) allows selection of either a high or low gain range which differ by a factor of 10. The signals are subsequently fanned out by the driver
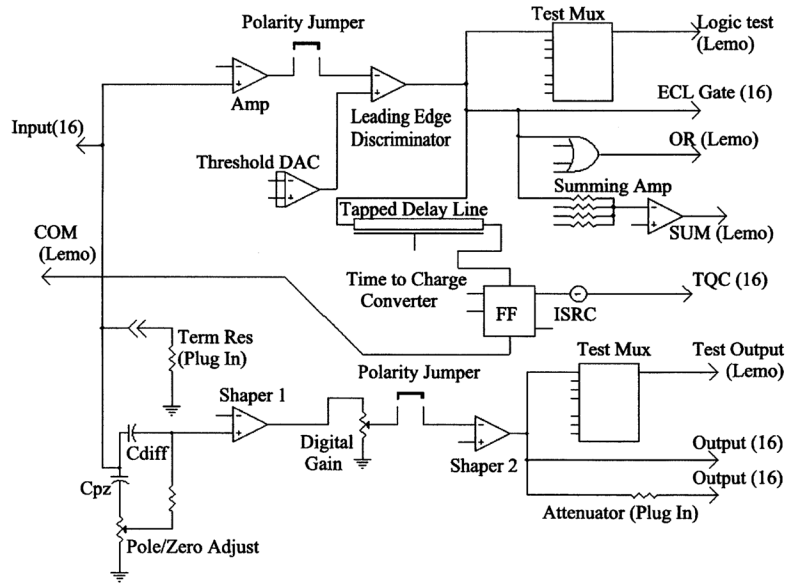
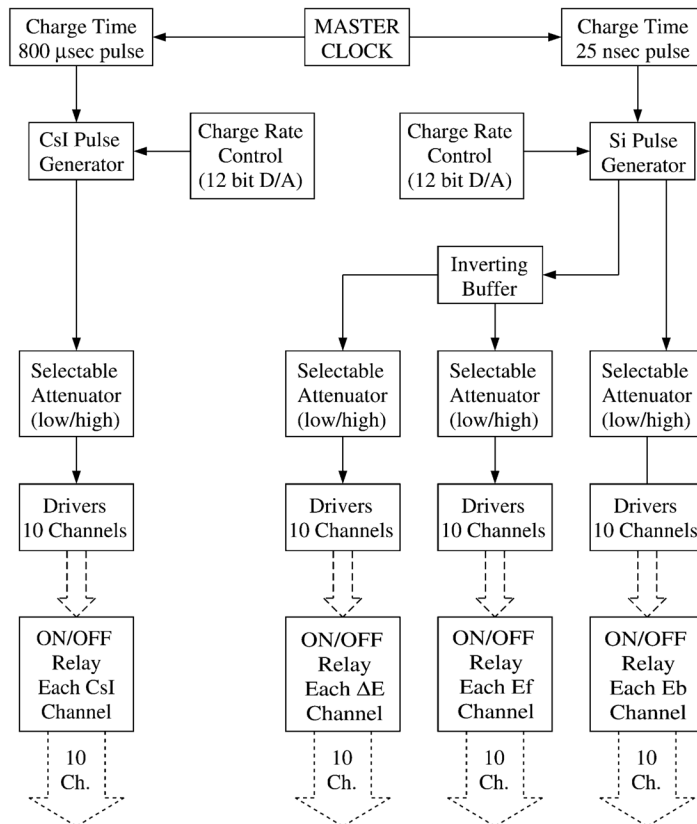Fig. 9. Functional block diagram of silicon processor module.

Fig. 10. Functional block diagram/schematic of IU pulser.

electronics to 10 pulser channels each. Each pulser channel has a remotely controllable relay on the output and has sufficient power to drive 16 pre-amplifiers without loading effects. The pulse frequency is selectable from 0.5 to 100 Hz. All functions of the pulser, including the amplitude of the pulse for any pulser channel and the ON/OFF state of the output relay, can be varied under computer control via an RS-232 serial interface. During the course of an experiment, the pulser can be operated in "picket-fence mode". In this mode, the pulse amplitude is incremented automatically every 1000 pulses in order to span the entire dynamic range of the electronic channel. Thus, both the gain and linearity of all electronic channels are measured continuously. Moreover, changes in electronic noise can be distinguished from radiation damage to the Si detector. All pulses generated by the IU pulser were identified by a bit in the data stream, allowing separation of these events in the offline analysis. The IU pulser also facilitates gain matching of electronic channels during the start-up phase of an experiment.

Due to the long duration of some of the experiments, a major concern was the extent to which the IU pulser could track changes in electronic gain. The stability achieved during a recent experiment is depicted in Fig. 11. In this figure, the percent change in the fitted slope relating the Si ADC channel to the IU pulser amplitude is plotted as a function of time. The four panels in Fig. 11 show increasing sensitivity to variations in gain. Evident in panel (a) (the largest gain variations) are three different regions of gain. Each of these regions corresponds to a different non-contiguous part of the experiment. These gain changes were manually selected during the experiment. Within each region the gain is relatively constant. In panel (b) a somewhat different pattern is observed. Over the interval 1000–3000 min the gain changes steadily. After this interval it remains relatively constant. A somewhat similar behavior is observed in panel (c) with a higher level of sensitivity. Finally, panel (d) shows a trend in gain change that is constant within the sensitivity of the gain change determination. From this figure, we deduce that electronic changes in gain can be monitored at the 0.02% level.
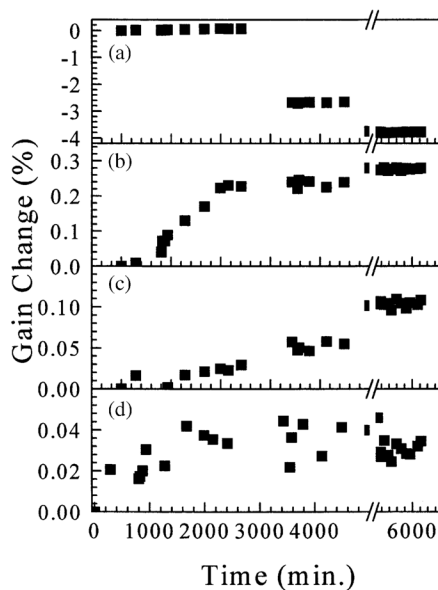

Fig. 11. Stability as measured by IU pulser.

5. Overview of LASSA data acquisition

An overview of the LASSA electronics can be seen in Fig. 12. Analog signals for the Si and CsI(Tl)/PD detectors processed by the processor module were digitized in Phillips Scientific peak-sensing ADCs (7164H) or Lecroy 4300B Fast Encoding Readout ADCs. A total of thirty 16-channel ADCs and nine FERA modules were required to read out all the signals from LASSA. Readout of this relatively large number of electronic channels was facilitated by a non-standard readout technique to improve upon what is attainable under the CAMAC standard for the Phillips 7164H.

The Phillips 7164H CAMAC ADCs were read out using a specially designed CAMAC-to-FERA protocol converter SS32 [24]. Utilizing its intrinsic intelligence, every converter executed a hit-pattern-based sparse readout of up to 24 ADCs via the standard CAMAC protocol. The data were then immediately transferred via a front panel 16-bit ECL port to the remote FERA receiver, pursuant to the Lecroy FERA handshaking protocol. Limited by the ADC access time, the readout of the Phillips ADCs proceeded at a rate
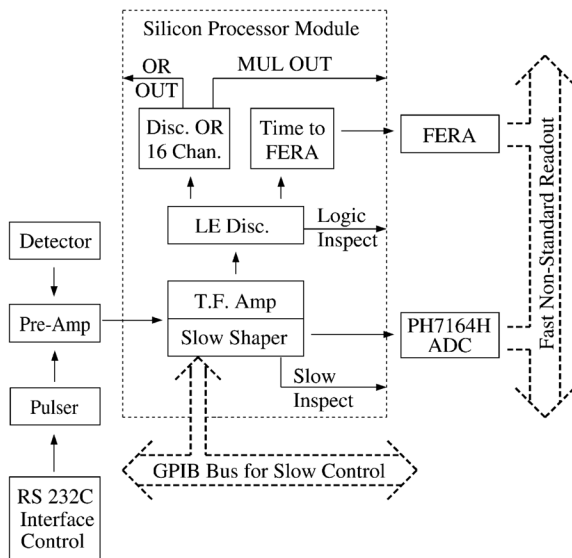
Fig. 12. Functional block diagram of the electronics.

of approximately 3 MHz. This non-standard readout, which required no hardware modifications to the 7164H ADCs, the CAMAC crates or controllers, resulted in a 7.5-fold reduction in the readout time of the LASSA electronics as compared to a standard CAMAC readout.

6. Calibration

Calibration of the LASSA modules consists of three parts: calibration of ΔE_{65} Si strips with an α-particle source, calibration of all electronic channels with a precision charge pulser into the detector input, and calibration of the telescopes with direct beam. Depending upon the goal of the experiment, e.g. if isotopic identification beyond $Z = 4$ is not required nor is good absolute energy determination for energetic light particles, the complexity of the in-beam calibration can be minimized or perhaps omitted altogether. The most demanding requirements are isotopic identification for $Z \geqslant 5$ and calibration of the CsI(Tl) for energetic particles. These requirements necessitate an in-beam calibration. An example of such a calibration procedure, performed with the Michigan State K1200-A1200 cyclotron/magnetic ana-

lysis system following a series of experiments, is described below.

Immediately following the last experiment, the LASSA array was calibrated in three stages. The first stage involved calibration of the device in the running configuration with a precision pulser and a charge terminator. In the second stage, a series of fragmentation beams was used and each detector was repositioned to allow the beam to be put directly into the telescope. Beams of 20 MeV/u ^{16}O and 40 MeV/u ^{36}Ar were accelerated by the K1200 cyclotron at Michigan State University and used to bombard a production target at the exit of the cyclotron. Reaction products from projectile fragmentation were subsequently selected according to magnetic rigidity by the A1200 magnetic channel. These low intensity secondary beams ($\sim$1300 p/s) were then used to directly scan the detector face. The beams used are listed in Table 2. These beams were useful in correcting the thickness non-uniformity of the 65 μm Si detector, as well as in calibrating both of the Si detectors and the CsI(Tl) detector. Finally, following the fragmentation beams, a ^{228}Th α-particle source was used to calibrate the 65 μm detectors.

6.1. Thickness non-uniformity correction for the 65 μm detector

Following the energy calibration of the LASSA 65 and 500 μm detectors using the information provided by the precision charge pulser (Ortec 448) and the ^{228}Th α-particle source, the observed isotopic resolution is rather poor, as illustrated in Fig. 13. However, we had previously determined that the intrinsic isotopic resolution of such Si strip detectors is better than the result shown in Fig. 13. We had established this fact by an in-beam test of a prototype telescope carried out at Texas A & M University's Cyclotron Institute.

When one constructs a ΔE–E map (ΔE_{65}–EF$_{500}$) selected on one particular "pixel" (the intersection of a given front and back strip in the 500 μm detector) for the prototype telescope, one observes isotopic resolution of carbon isotopes, limited only by the counting statistics. These results suggested a thickness variation of the prototype 65 μm wafer

Table 2
Secondary beams produced by projectile fragmentation used in the calibration of LASSA

^{16}O fragmentation products	E (MeV)	^{36}Ar fragmentation products	E (MeV)	^{36}Ar fragmentation products	E (MeV)
p	77.62	p	151.1	^{18}F	719.8
d	40.00	d	79.98	^{19}F	683.4
t	26.82	t	53.94	^{20}F	650.4
^{3}He	105.8	^{3}He	210.0	^{20}Ne	799.8
^{4}He	80.00	^{4}He	160.0	^{22}Na	879.8
^{6}He	53.65	^{6}He	107.9	^{23}Na	843.0
^{6}Li	120.0	^{6}Li	239.9	^{24}Na	809.1
^{7}Li	103.2	^{7}Li	206.8	^{24}Mg	959.8
^{8}Li	90.42	^{8}Li	181.6	^{25}Mg	922.9
^{7}Be	182.3	^{7}Be	363.4	^{26}Mg	888.7
^{9}Be	142.5	^{9}Be	285.6		
^{10}Be	128.5	^{10}Be	257.9		
^{8}B	248.5	^{10}B	399.9		
^{10}B	200.0	^{11}B	364.9		
^{11}B	182.2	^{12}B	335.4		
^{9}C	317.4	^{11}C	521.5		
^{10}C	286.7	^{12}C	479.9		
^{11}C	261.3	^{13}C	444.3		
^{12}C	240.0	^{14}C	413.6		
^{13}C	221.9	^{13}N	601.0		
^{12}N	325.4	^{14}N	559.9		
^{13}N	301.0	^{15}N	523.9		
^{14}N	280.0	^{16}N	492.3		
^{13}O	391.7	^{15}O	680.6		
^{14}O	364.6	^{16}O	639.8		
^{15}O	340.8	^{17}O	603.6		
^{16}O	320.0	^{18}O	571.2		

across its face. This finding is consistent with results obtained for the non-planarity of thin Si detectors [21,25].

Since the energy loss a particle experiences in traversing the detector is proportional to the detector thickness, it is crucial to correct for the thickness non-uniformity of the 65 μm detector. Therefore, in analyzing data from the LASSA detectors, we first determined the change in thickness along a single strip of the LASSA ΔE_{65} detector. All pixels along a strip are associated with the same electronic channel and hence the deduced thickness variation is calibration independent. To determine the thickness variation along a strip, we used fixed points in the residual energy in the 500 μm detector (EF$_{500}$) of α particles and determined the associated energy loss in the transmission detector (ΔE_{65}) for each of the pixels in the strip. Once the thickness variation along a strip was corrected, we were able to utilize the same technique for isotopically identifying fragments through boron. We parameterized the matching factors obtained in this way as a function of ΔE_{65} (MeV). As a result of this procedure, variations in the calibration between strips, as well as the thickness variation between strips, are minimized. The two-dimensional correction matrix we obtained in this way is shown in Fig. 14. The X and Y position shown in the figure reflect the EF$_{500}$ and EB$_{500}$ strips in the 500 μm detector, respectively. Along a strip in the ΔE detector (constant value of X as the strips in the ΔE_{65} and EF$_{500}$ run in the same direction), the variation reflects simply the thickness variation of the 65 μm detector. Between strips one is sensitive to both the thickness variation of the 65 μm

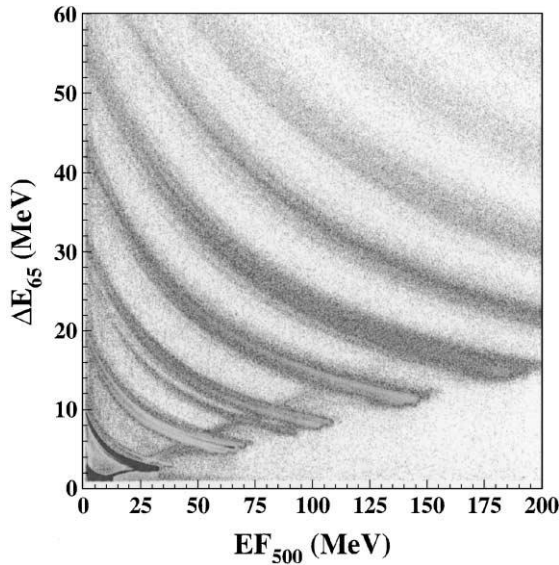Fig. 13. 2D of Si–Si before thickness correction of the 65 μm detector.

Fig. 14. 2D map of thickness correction factors for 65 μm detector.

detector, as well as to small residual electronic variations (subsequent to calibration) between different electronic channels. The matching procedure using this matrix resulted in the two-dimensional $\Delta E–E$ spectrum (ΔE_{65}–EF_{500}) displayed in Fig. 15. This mapped spectrum clearly shows isotopic resolution through nitrogen and is representative of all nine telescopes in LASSA. A comparison of Fig. 13 with Fig. 15 illustrates the crucial importance of correcting for the thickness variation in the 65 μm detector in achieving optimal particle identification. The spectrum shown in Fig. 15 is for all particles that do not have a CsI(Tl)/PD signal; i.e. particles that either stop in the 500 μm Si or "punch-through" 500 μm Si but somehow escape the CsI(Tl) crystals behind the silicon detector. The background haze visible in Fig. 15 is due to particles passing through inactive regions (edges, interstrips, etc.) of the telescope, resulting in inconsistent ΔE_{65}–EF_{500} combinations. Also visible in Fig. 15 is a faint band of particles with a positive slope between He and Li. Particles in this band "punch-through" the 500 μm Si detector and consequently that signal is effectively a ΔEF_{500} signal. These particles are present due to a slight mis-alignment of the Si detectors relative to the CsI(Tl) crystals, as well as
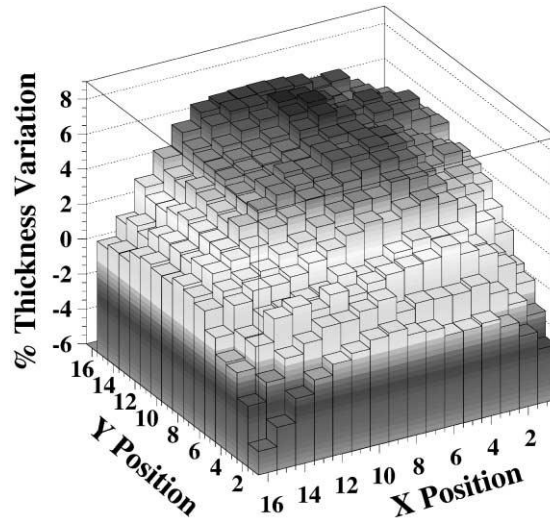
to the dead area between adjacent CsI(Tl) crystals (due to wrapping for the purpose of optical isolation). One is able to eliminate this contribution, at the expense of geometric efficiency, by gating selectively on the position in the Si detectors.

6.2. Thickness determination for the 500 μm detector

Using the fragmentation data, a two-dimensional $\Delta E–E$ spectrum (EF_{500}–E_{CsI}) of the Si–CsI(Tl) was constructed for each telescope and the centroids in EF_{500} were determined for all identifiable isotopes. Since the Z, A and incident energy of these ions (selected by the magnetic channel) is known, the energy deposited in the 500 μm detector could be calculated with an energy loss program, TRIM [26], for different input values of the detector thickness. The effective thickness of the detector was determined by minimizing the difference between the calculated energy loss and the measured energy loss as a function of thickness. The effective thicknesses deduced in this manner for the nine telescopes are summarized in Table 3. Also shown, for reference, in Table 3 are the nominal thicknesses quoted by the manufacturer. These nominal thicknesses were determined by measuring, by mechanical means,
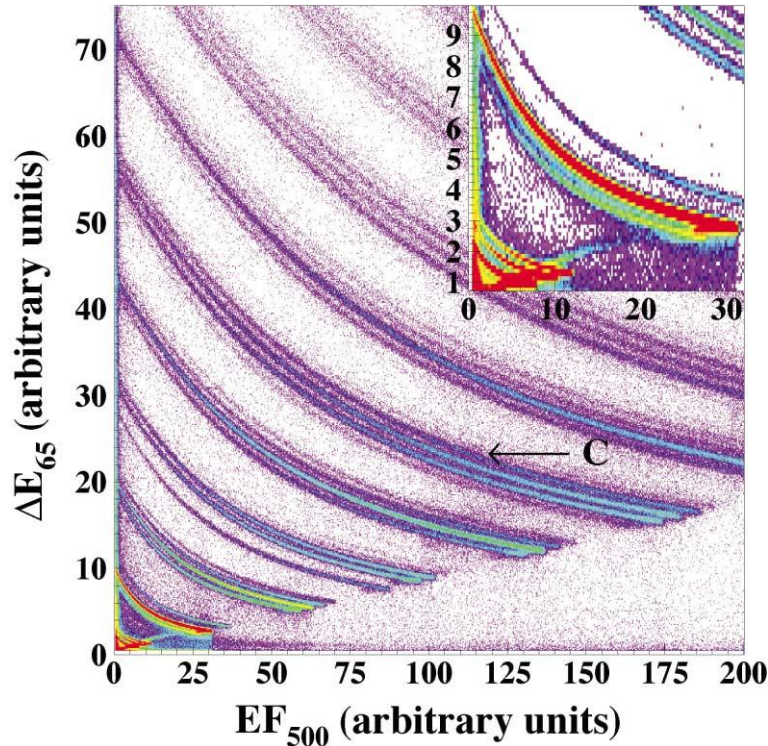
Fig. 15. 2D of Si–Si following thickness correction of the 65 μm detector.

Table 3
Nominal and deduced thicknesses of the 500 μm LASSA Si strip detectors

Detector	1	2	3	4	5	6	7	8	9
Nominal thickness (μm)	510	499	471	461	468	481	456	482	476
Deduced thickness (μm)	494	481	460	442	456	464	453	461	454

an outer section of the silicon wafer from which a detector was cut. Based on our previous work [21], it is not surprising that the silicon detectors are 15 μm thinner on average than their nominal values. Subsequent energy calibration of the CsI(Tl) utilizes the deduced thicknesses.

6.3. Isotopic resolution in the Si–CsI(Tl)

To identify particles that stopped in the CsI(Tl) crystal, the EF_{500} signal of the 500 μm detector was chosen due to the superior PA used for these signals, as compared with EB_{500}. The EB_{500} signals were used with higher gain shaping amplifiers to improve the identification of the isotopes of

hydrogen at the expense of dynamic range. The primary purpose of the EB_{500} signals was for position determination.

Following calibration of the EF_{500} signals with a precision charge pulser two-dimensional ΔE–E maps (EF_{500}–E_{CsI}) were generated summed over the pixels in a demi-strip. A demi-strip corresponds to the half of an EF_{500} strip in front of a single CsI(Tl) crystal. In a procedure analogous to the analysis of the ΔE_{65}–EF_{500}, we generated matching factors by determining the ΔE for fixed values of $Z, A,$ and CsI(Tl) light output. By examining the light output in different demi-strips associated with different fragments from the fragmentation beams, we deduced that the light

output of the CsI(Tl) did not manifest a significant global trend as a function of position. Local variations measured by penetrating α particles have been reported previously [27]. By this matching procedure we were able to produce a matched EF_{500}–E_{CsI} spectrum for each crystal. Different CsI(Tl) crystals within a telescope were subsequently matched by utilizing the fragmentation beams. A typical EF_{500}–E_{CsI} two-dimensional spectrum for a telescope is shown in Fig. 16. The isotopes of oxygen can be clearly distinguished. The background haze visible in Fig. 16 has two origins. Particles passing through the inactive regions of the telescope give rise to spurious EF_{500}–E_{CsI} combinations. Coincidence summing within a CsI(Tl) crystal is particularly evident in the low EF_{500} region. Double-hits of a neutron or high energy proton with a second particle in a single CsI(Tl) crystal distort the E_{CsI} signal. Assignment of the isotopically resolved bands (PID: particle identification lines) was further checked by comparison

with the fragmentation beams, resulting in no uncertainty in associating a given locus with a particular isotope.

A more quantitative measure of the isotopic resolution achieved is depicted in Fig. 17. In this figure, the isotopic distributions for carbon and oxygen fragments resolved in the ΔE_{65}–EF_{500} and the EF_{500}–E_{CsI} are shown. These spectra are summed over all nine telescopes in LASSA. In the Si–CsI(Tl) carbon PID spectrum (panels c and d), one can resolve all isotopes from ^{10}C to ^{16}C. Separation of ^{10}C from ^{11}C is somewhat worse in the Si–Si PID spectrum (panels a and b). In the oxygen PID spectra isotopes from ^{15}O to ^{20}O are clearly visible. This excellent particle identification meets the design criteria for the array. The isotopic resolution achieved by LASSA facilitates studies of mirror nuclei. For example, the isotopic resolution achieved allows examination of the $^{8}Li/^{8}B$, $^{10}Be/^{10}C$, $^{13}C/^{13}N$, and $^{15}N/^{15}O$ mirror nuclei in addition to previously studied pairs.
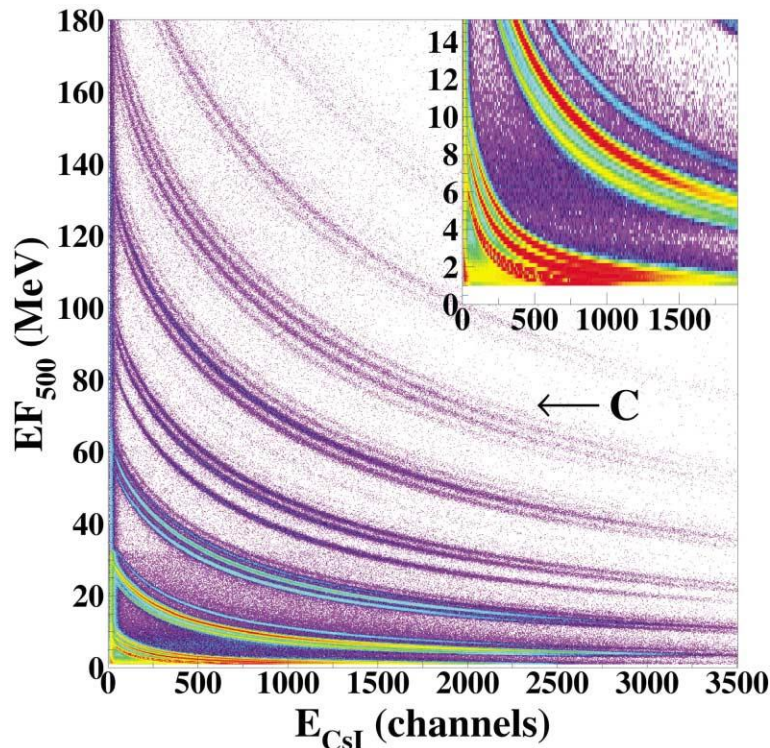

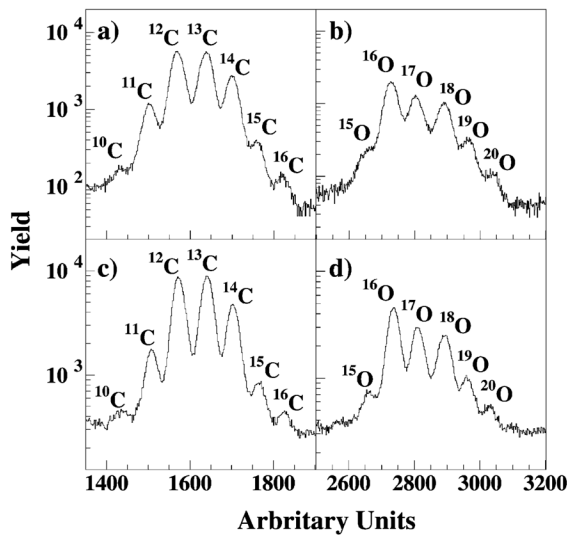Fig. 16. 2D of Si–CsI(Tl) for a telescope in LASSA.

Fig. 17. Panels (a) and (b) depict the isotopic distributions for C and O, respectively, in the Si–Si portion of the telescope. Panels (c) and (d) depict the isotopic distributions for C and O, respectively, in the Si–CsI(Tl) portion of the telescope. These spectra are summed over all nine telescopes in LASSA.

Fig. 18. Light output of CsI(Tl) as a function of Z, A, and E.

7. Energy calibration of the CsI(Tl)

To calibrate the CsI(Tl) crystals in energy, we used the two-dimensional spectra (EF_{500}–E_{CsI}), an example of which is shown in Fig. 16. For fixed E_{CsI} (channel number) and each of the isotopes identified, the corresponding energy in the 500 μm detector (EF_{500}) was determined. Using the energy deposited in the 500 μm detector, the corresponding energy deposited in the CsI(Tl) crystal was calculated using TRIM [26]. (This approach works well when a significant change in EF_{500} is associated with a finite change in E_{CsI}.) The light output (LO) response arrived at in this way is shown in Fig. 18 for a typical telescope. Open circles and open squares denote the PID line data extracted from the ΔE–E maps (EF_{500}–E_{CsI}) for ^{11}C and ^{14}C, while asterisks represent the data provided by the fragmentation beams (Table 2). A clear mass dependence is evident, particularly at high energy. In the right-hand panel of Fig. 18, the fragmentation data is fit using the parameterization of Larochelle et al. [28] and the resulting curves for ^{11}C, ^{12}C, ^{13}C, and ^{14}C are shown. As can
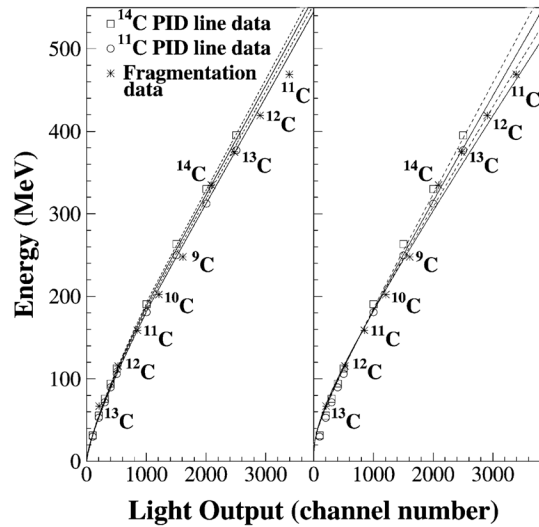
be seen in this right-hand panel, the fits do not describe the data extracted from the PID lines (open symbols), particularly at low values of the light output. These differences may be due to temperature variations in the CsI(Tl) crystals (although the detector housing is actively cooled) as the calibration with the fragmentation beams was conducted following the experiment and the CsI(Tl) may not have had sufficient time to temperature equilibrate prior to the calibration.

In the left-hand panel of Fig. 18, we show the result of fitting the PID line data with a two part fit. For the low energy portion of the calibration (LO ≤ 1000) the formalism described in Ref. [29] was used, however, each isotope was calibrated independently as this formalism has no explicit mass dependence. In the high energy region (LO ≥ 1000), the formalism described in Ref. [28] was used as this formalism has an explicit mass dependence. The two fit regions were "feathered" together in a linear fashion over the interval 900–1100. This procedure yielded the best fit of the PID line data. As can be seen in the left-hand panel, this calibration is in reasonably good agreement with the fragmentation data at low energies, but overpredicts the energy for large values of the light output. This difference between the fragmentation and characteristic line data can
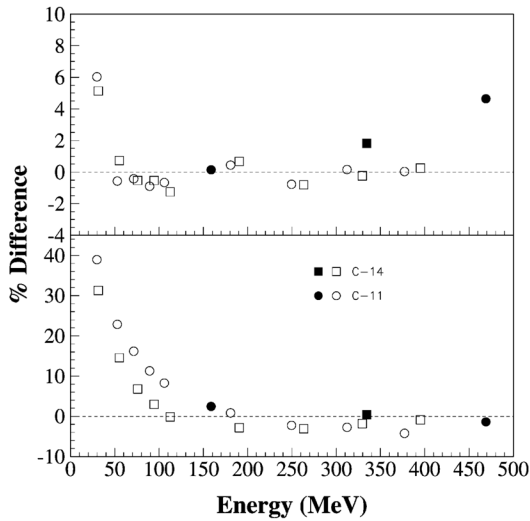
Fig. 19. Percent deviation of the fragmentation and PID calibration data from the respective fits. See text for details.

be used as an estimate of the absolute uncertainties involved in the CsI(Tl) calibration.

To quantitatively examine the absolute uncertainties in the CsI(Tl) calibration, we have constructed the percent deviation of the data from the fits shown in Fig. 18. The percent deviation from the fit to the PID line data alone is shown in the top panel of Fig. 19. The corresponding case in which the fragmentation data alone has been fit is shown in the bottom panel of the figure. In the top panel, a maximum deviation of 5% is observed at the highest incident energy for the fragmentation data. In the lower panel, where one relies on the fragmentation data alone for the light output calibration, the percent deviation is as large as 40% at low energy. Part of the difficulty in relying upon the fragmentation data alone is the restricted range in which these data were measured and the limited number of constraining points. In addition, the large deviation shown in the lower panel is amplified because it is examined in relative rather than absolute terms. The uncertainty associated with energy loss calculations for particles that just punch through the 500 μm detector may also play a role in amplifying this difference. Nevertheless, this plot emphasizes the difficulty in performing an absolute calibration to the sub-percent level (as has been achieved with the Si detectors) with

detectors that are both non-linear and have a temperature sensitive response function.

From the isotopic resolution we have achieved, we estimate the uncertainty in relative calibration between different Si strips and electronic channels to be $\sim 0.5\%$, however, the uncertainty in absolute calibration (due to the CsI) is considerably larger ~ 2–5%.

8. Summary

We have designed and developed a new, low-threshold charged particle detector array, LASSA. Each element of the array consists of a Si–Si–CsI(Tl) telescope. The silicon detectors are segmented into strips and provide an angular resolution of $\sim 0.9^\circ$. In order to minimize the dead area and allow close-packing of the telescopes in the array, a compact frame for the silicon detectors with an integrated, low-profile cable was developed. Dedicated high density electronics for the array consisting of pre-amplifiers, fast and slow amplifiers, dicriminators, and time-to-charge converters were also developed. With these electronics, an energy resolution of $\leqslant 0.5\%$ was obtained for the silicon detectors. Following correction for thickness variation of the 65 μm Silicon detector, isotopic identification for charged particles with $Z \leqslant 8$ was achieved.

Acknowledgements

References

[1] H. Muller, B. Serot, Phys. Rev. C 52 (1995) 2072.
[2] L.G. Sobotka, Phys. Rev. C 50 (1994) R1272.

[3] J.F. Dempsey, R.J. Charity, L.G. Sobotka, G.J. Kunde, S. Gaff, C.K. Gelbke, T. Glasmacher, M.J. Huang, R.C. Lemmon, W.G. Lynch, L. Manduci, L. Martin, M.B. Tsang, D.K. Agnihotri, B. Djerroud, W.U. Schroder, W. Skulski, J. Toke, W.A. Friedman, Phys. Rev. C 54 (1996) 1710.

[4] M. Colonna, M. di Toro, G. Fabris, S. Maccarone, Phys. Rev. C 57 (1998) 1410.

[5] Bao-An Li, C.M. Ko, Phys. Rev. C 57 (1998) 2065.

[6] F. Rami, Y. Liefels, B. de Schauenburg, A. Gobbi, B. Hong, et al., Phys. Rev. Lett. 84 (2000) 1120.

[7] R. LaForest, E. Ramakrishnan, D. Rowland, A. Ruangma, E.M. Winchester, E. Martin, S.J. Yennello, Phys. Rev. C 59 (1999) 2567.

[8] R. Nebauer, J. Aichelin, the INDRA collaboration, Nucl. Phys. A 658 (1999) 67.

[9] R. Trockel, U. Lynen, J. Pochodzalla, W. Trautmann, N. Brummund, E. Eckert, R. Glasow, K.D. Hildebrand, K.H. Kampert, W.F.J. Muller, D. Pelte, H.J. Rabe, H. Sann, R. Santo, H. Stelzer, R. Wada, Phys. Rev. Lett. 59 (1987) 2844.

[10] Y.D. Kim, R.T. de Souza, D.R. Bowman, N. Carlin, C.K. Gelbke, W.G. Gong, W.G. Lynch, L. Phair, M.B. Tsang, F. Zhu, S. Pratt, Phys. Rev. Lett. 67 (1991) 14.

[11] H.F. Xi, G.J. Kunde, O. Bjarki, C.K. Gelbke, R.C. Lemmon, W.G. Lynch, D. Magestro, R. Popescu, R. Shomin, M.B. Tsang, A.M. Vandermolen, G.D. Westfall, G. Imme, V. Maddalena, C. Nociforo, G. Raciti, G. Riccobene, F.P. Romano, A. Saija, C. Sfienti, S. Fritz, C. Gross, T. Odeh, C. Schwarz, A. Nadasen, D. Sisan, K.A.G. Rao, Phys. Rev. C 58 (1998) R2636.

[12] E. Cornell, T.M. Hamilton, D. Fox, Y. Lou, R.T. de Souza, C. Schwarz, M.J. Huang, D.R. Bowman, J. Dinius, C.K. Gelbke, T. Glasmacher, D.O. Handzy, W.-C. Hsi, M.A. Lisa, W.G. Lynch, G.F. Peaslee, L. Phair, M.B. Tsang, C. Williams, G. van Buren, R.J. Charity, L.G. Sobotka, W.A. Friedman, Phys. Rev. Lett. 75 (1995) 1475.

[13] E. Cornell, T.M. Hamilton, D. Fox, Y. Lou, R.T. de Souza, M.J. Huang, W.-C. Hsi, C. Schwarz, C. Williams, D.R. Bowman, J. Dinius, C.K. Gelbke, D.O. Handzy, M.A. Lisa, W.G. Lynch, G.F. Peaslee, L. Phair, M.B. Tsang, G. VanBuren, R.J. Charity, L.G. Sobotka, Phys. Rev. Lett. 77 (1996) 4508.

[14] S. Albergo, et al., Nuovo Cimento 89 (1985) 1.

[15] J. Pochodzalla, T. Moehlenkamp, T. Rubehn, A. Schuttauf, A. Worner, E. Zude, M. Begemann-Blaich, Th. Blaich, H. Emling, A. Ferrero, C. Gross, G. Imme, I. Iori, G.J. Kunde, W.D. Kunze, V. Lindenstruth, U. Lynen, A. Moroni, W.F.J. Muller, B. Ocker, G. Raciti, H. Sann, C. Schwarz, W. Seidel, V. Serfling, J. Stroth, W. Trautmann, A. Trzcinski, A. Tucholski, G. Verde, B. Zwieglinski, Phys. Rev. Lett. 75 (1995) 1040.

[16] Hamamatsu Photonics K.K., 360 Foothill Rd., Bridgewater, N.J. 08807, USA.

[17] Micron Semiconductor Ltd., 1 Royal Bldg, Marlborough Rd., Lancing, Sussex, UK BN15 8UN.

[18] Rogers Corp., Circuit Materials Division, 100 N. Dobson Rd., Chandler, AZ 85224, USA.

[19] Printed Circuit Board prototype fabrication facility, Direct Imaging of Vermont, Inc., 30 A Street, P.O. Box 820, Wilder, VT 05088.

[20] SIFCO Selective Plating, 5708 Schaaf Road, Cleveland, OH 44131, USA.

[21] D. Fox, R.T. de Souza, S.L. Chen, B. Davin, T.M. Hamilton, J. Dorsett, J. Ottarson, Nucl. Instr. and Meth. A 368 (1996) 709.

[22] Available from Pico Systems, 543 Lindeman Rd., St. Louis, MO 63122.

[23] Electronic Instrument Services, Department of Chemistry, Indiana University, Bloomington.

[24] J. Toke, DOE Report ER-40414, University of Rochester, 1998, p. 160.

[25] B. Davin, Ph.D. Thesis, Indiana University, 2001.

[26] TRIM, J.F. Ziegler, http://www.research.ibm.com/ion-beams/home.htm.

[27] A. Wagner, W.P. Tan, K. Chalut, R.J. Charity, B. Davin, Y. Larochelle, M.D. Lennek, T.X. Liu, X.D. Liu, W.G. Lynch, A.M. Ramos, R. Shomin, L.G. Sobotka, R.T. de Souza, M.B. Tsang, G. Verde, H.S. Xu, Nucl. Instr. and Meth. A 456 (2001) 290.

[28] Y. Larochelle, L. Beaulieu, B. Djerroud, D. Dore, P. Gendron, E. Jalbert, R. Laforest, J. Pouliot, R. Roy, M. Samri, C. St-Pierre, Nucl. Instr. and Meth. A 348 (1994) 167.

[29] P.F. Mastinu, P. Milazzo, M. Bruno, M. D'Agostino, L. Manduci, Nucl. Instr. and Meth. A 338 (1994) 419.